

See discussions, stats, and author profiles for this publication at: <https://www.researchgate.net/publication/230576980>

Density-Dependent Electrochemical Properties of Vertically Aligned Gold Nanorods

ARTICLE in THE JOURNAL OF PHYSICAL CHEMISTRY C · APRIL 2010

Impact Factor: 4.77 · DOI: 10.1021/jp912231s

CITATIONS

15

READS

43

4 AUTHORS:



Mariana Chirea

Koc University

21 PUBLICATIONS 312 CITATIONS

SEE PROFILE



João Borges

University of Minho

29 PUBLICATIONS 145 CITATIONS

SEE PROFILE



Carlos Pereira

University of Porto

108 PUBLICATIONS 1,543 CITATIONS

SEE PROFILE



A Fernando Sousa Silva

University of Porto

162 PUBLICATIONS 2,210 CITATIONS

SEE PROFILE

Density-Dependent Electrochemical Properties of Vertically Aligned Gold Nanorods

Mariana Chirea,* João Borges, Carlos M. Pereira, and A. Fernando Silva

CIQ-UP L4, Faculdade de Ciências, Universidade do Porto, Rua do Campo Alegre, 687, 4169-007 Porto, Portugal

Received: December 29, 2009; Revised Manuscript Received: April 9, 2010

Gold nanorods (AuNRs) with an aspect ratio of 2.33 or 3.16 were self-assembled onto 1,6-hexanedithiol-modified gold electrodes based on covalent interaction at a solution temperature of 35 °C. The formation of the 1,6HDT/AuNR bilayers as a function of the nanorods' adsorption time was studied by atomic force microscopy and quartz crystal microbalance, whereas their physical properties and chemical bonding were studied by contact angle and FT-IRRAS spectroscopy measurements. It was found that both types of nanorods were covalently bonded to the Au-1,6HDT-SAM modified electrodes in an end topography and with a high surface density. The electrochemical properties of the Au-1,6HDT-AuNR modified electrodes, as a function of the nanorods' adsorption time, were studied by cyclic voltammetry, square wave voltammetry, and electrochemical impedance spectroscopy using $[\text{Fe}(\text{CN})_6]^{3-/4-}$ as the redox probes. The highest enhancement of the electrical current in the cyclic voltammograms was recorded at the Au-1,6HDT-AuNR modified electrodes for 7 h of chemisorption of 2.33 aspect ratio rods or 15 h of chemisorption of 3.16 aspect ratio rods. The high decrease of the apparent charge-transfer resistance upon nanorod self-assembly suggests a charging of the rods by the $[\text{Fe}(\text{CN})_6]^{3-/4-}$ in solution and electron transfer across them. Moreover, the variation of the tunneling parameter β suggests that the electron tunneling process through the 1,6HDT molecules is more efficient at the electrodes modified with bilayers containing short rods ($\beta = 0.78 \pm 0.08 \text{ \AA}^{-1}$ /per methylene unit) than at the electrodes modified with bilayers containing long rods ($\beta = 0.84 \pm 0.10 \text{ \AA}^{-1}$ /per methylene unit). The self-assembly of the AuNRs in an end-bonding topography with a high surface coverage restored almost completely the electronic communication that was entirely blocked by the preceding 1,6HDT layer.

1. Introduction

The stepwise self-assembly of nanomaterials onto various electrodes has recently received considerable interest as a consequence of the rapid progress in nanotechnology research and applications.^{1–3} The self-assembly method allows the fabrication of 3D superstructures of linked nanoparticles (NPs) by stepwise immersion of the substrates in various solutions. The versatility of this method is based on a large variety of interactions, such as electrostatic, hydrogen bonding, covalent bonding, or coordinate bonding.^{4–6} For example, Brust et al.^{7–9} were among the first to prepare covalently cross-linked gold nanoparticle–molecule assemblies by functionalization of a glass substrate with a monolayer of 3-(mercaptopropyl) trimethoxysilane (MPTMS) and consecutive immersion in thiol-free 6 nm gold nanoparticle (Au NP) solution for 12 h, generating a first AuNP layer. Successively, they attached α,ω -alkanedithiols ($\text{HS}(\text{CH}_2)_n\text{SH}$, $n = 6, 9, 12$) to the AuNP layer by repeated immersions of the substrate into NP and dithiol solutions and rinsing between immersions. Following this procedure, they have fabricated AuNP thin films with nonmetallic optical and electronic properties.^{8,9} Other authors, for example, Leibowitz et al.,¹⁰ demonstrated that a place exchange reaction can be used to prepare cross-linked NP assemblies. They mixed solutions of alkanethiolate-capped NPs (e.g., decanethiolate-capped Au NP) and excess dithiol cross-linkers (e.g., 1,9-nonanedithiol) and immersed a solid substrate into the mixture. Exchange between the ligand shell of NPs and the free dithiol linker has led to precipitation of cross-linked NPs on the substrate.¹⁰ The stable attachment of NPs to any type of

substrate is a critical step in the development of devices that exploit their properties, such as size, morphology, large surface area, and possible quantum confinement.¹¹ The films containing nanoparticles are very useful for electrocatalytic and electroanalytical applications, and in consequence, the detailed knowledge of their electrochemical properties is very important. Within nanoparticles' films, the electron transfer takes place by hopping or tunneling between adjacent NPs and the film conductivity depends on the length and nature of the encapsulating molecules.^{2,12–18} The nanoparticles improve the conductivity of the films in which they are incorporated, and these electrocatalytic properties are initially enhanced by increasing the number of NP layers but level off in thicker films.^{12–18} The electrochemical behavior of electroactive species in solution is rather complex on electrodes covered with these multilayers and depends not only on the nature of the outermost layer but also on the composition of the whole multilayer.^{1–3,12–18} For example, in a previous published work, we have used the capillary membrane model to describe the electrochemical and permeation properties of AuNP–polyelectrolyte films.¹⁶ We have studied the electrochemical responses of $[\text{Fe}(\text{CN})_6]^{4-}$ and $[\text{Ru}(\text{NH}_3)_6]^{3+}$ on Au NP (encapsulated by mercaptosuccinic acid)/polylysine multilayers, and we have demonstrated that both the nature of the outermost layer and the electroactive species affect the behavior. These results were attributed to different charge percolation pathways involving ionic diffusion through capillaries and pores and subsequent charge transfer via Au NPs.¹⁶ Ohsaka et al. demonstrated that citrate-stabilized AuNP immobilized on gold electrodes through 1,4-benzenedimethanethiol (BDMT) achieved good electrical communication with the underlying electrode surface despite the insulating effect of each BDMT layer. These AuNP layers showed a good electrocatalytic

* To whom correspondence should be addressed. E-mail: mariana.chirea@fc.up.pt. Tel: +351220402634. Fax: +351220402659.

activity toward oxygen reduction.¹⁸ The above-mentioned studies were focused on the electrochemical properties of spherical nanoparticles self-assembled into thin films. A new challenge in the nanotechnology research is the fabrication and characterization of films containing anisotropic nanomaterials, such as nanorods, nanostars, nanowires, and nanotubes. The shape of these anisotropic nanomaterials will have an additional effect on their electronic properties, as it is already known that this parameter has an evident influence on their optical properties.^{19–23} Recently, our group has investigated the electrochemical properties of rod-shaped nanoparticles, namely, gold nanorods (AuNRs), self-assembled onto dithiol-modified gold electrodes.²⁴ These anisotropic nanomaterials have proven an electrochemical behavior dependent on their size and the type of surface bonding.²⁴ In this paper, we report the electrochemical properties of the self-assembled AuNRs as a function of their adsorption time and, in consequence, as a function of their surface density. The self-assembly of AuNRs on gold electrodes was performed using 1,6-hexanedithiol (1,6HDT) as a cross-linker molecule. Atomic force microscopy, quartz crystal microbalance, FT-IRRAS spectroscopy, and contact angle measurements were performed in order to characterize the 1,6HDT-AuNR bilayers. The electrochemical activity of the AuNR layers as a function of their adsorption time was evaluated by cyclic voltammetry, square wave voltammetry, and electrochemical impedance spectroscopy using $[\text{Fe}(\text{CN})_6]^{3-/4-}$ as redox probes.

2. Experimental Section

2.1. Chemicals. Hydrogen tetrachloroaurate(III) trihydrate ($\text{HAuCl}_4 \cdot 3\text{H}_2\text{O}$, 99.999%, Sigma Aldrich), cetyltrimethyl ammonium bromide ($\text{C}_{19}\text{H}_{42}\text{NBr}$, Sigma, 99%), sodium borohydride (NaBH_4 , 96%, Sigma Aldrich), silver nitrate (AgNO_3 , pa quality, Riedel-de Haën), L-ascorbic acid ($\text{C}_6\text{H}_8\text{O}_6$, 99%, Aldrich), 1,6-hexanedithiol ($\text{C}_6\text{H}_{14}\text{S}_2$, Fluka, 97%), methanol (CH_3OH , 99.8%, Sigma), potassium hexacyanoferrate(III), potassium hexacyanoferrate(II) (pa quality, Merck, NaClO_4), HClO_4 (70%, redistilled, 99.999%, Aldrich), H_2SO_4 (pure, Pronalab), and H_2O_2 (30%, Fluka) were used as received. Millipore filtered water (resistivity $>18 \text{ M}\Omega \cdot \text{cm}$) was used to prepare all aqueous solutions and for rinsing. Prior to use, all the glassware was cleaned with freshly prepared aqua regia ($\text{HNO}_3/\text{HCl} = 1:3$, % v/v), rinsed abundantly with Millipore water and dried.

2.2. Synthesis of Au NRs with Aspect Ratios of 2.33 and 3.16. The gold nanorods were synthesized following the seed-mediated method developed by El. Sayed et al.²⁵ The resulting rods were purified by solvent decantation and soft washing with Millipore water through centrifugation (centrifuge Galaxy, 3000 rpm, 5 min) and sonication (Bandeline Sonorex) for five times. The purified AuNRs were used for substrate modification at a concentration of 0.50 mg/mL (aqueous solution). TEM imaging analysis showed that the aspect ratios of the AuNRs were 2.33 for the first sample (AuNR₁, average length per width of 38.20 nm per 16.40 nm) and 3.16 (AuNR₂, average length per width of 50 nm per 15.82 nm) for the second sample (see Figures S1 and S2 in the Supporting Information).

2.3. Transmission Electron Microscopy. A drop of each rod solution was cast on copper carbon grids, let to dry for at least 24 h, and imaged. The TEM images were recorded with a transmission electron microscope, Hitachi 8100, equipped with a Rontec Standard EDS detector and digital images acquisition, operating at 200 kV and having a point resolution of 1.6 nm. Image J software was used for the evaluation of the aspect ratio of the rods (the average length/width ratio) from the TEM images.

2.4. UV-vis Spectroscopy. The UV-vis spectra of the AuNR samples were recorded on a Hitachi U-3000 spectrophotometer in the range of 200–900 nm, using quartz cuvettes with a 1 cm light path and freshly prepared AuNR solutions.

2.5. Quartz Crystal Microbalance Measurements. The QCM measurements were performed with a QCM-Z500 apparatus (KSV, Finland) that provided ΔF changes for six overtone frequencies (5, 15, 25, 35, 45, and 55 MHz). To monitor the in situ self-assembly of the layers, the following procedure was adopted: the QCM electrodes (gold-coated quartz crystals, 0.785 cm² area) were washed with freshly prepared piranha solution (3:1 mixture of concentrated sulfuric acid and hydrogen peroxide, 30%; *Caution! Piranha solution is corrosive and reacts violently with organic materials.*), followed by rinsing with large amounts of Millipore water, dried in a stream of nitrogen, and consecutively placed in the QCM cell. After mounting the crystal in the cell, a small amount of ethanol was introduced into the cell, and the frequency change was recorded over 20 min as a stable baseline. Next, the pure solvent was gently removed from the QCM cell and an ethanolic solution of 1,6-hexanedithiol (0.015 M) was injected into the cell (0.50 mL) after deaeration with nitrogen for 20 min. The frequency change was recorded continuously during the chemisorption process of 1,6HDT at a 25 °C solution temperature (Supporting Information, Figure S3). Next, the QCM electrode was removed from the reaction chamber and persistently washed with ethanol and Millipore water, dried in a stream of nitrogen, and further imaged by tapping mode AFM. After AFM imaging, the 1,6HDT-modified QCM electrode was reinserted in the QCM chamber and a second baseline was recorded for 20 min using Millipore water as the solvent. The substrate was further modified with gold nanorods by gentle injection of freshly prepared and purified AuNRs (0.50 mg/mL), setting the solution temperature at 35 °C. The resulting Au-1,6HDT-AuNR modified electrode was removed from the QCM cell, washed persistently with Millipore water, dried in a stream of nitrogen, and imaged in tapping mode AFM. The experiments were repeated three times, and similar results were obtained.

2.6. Atomic Force Microscopy Measurements. The resulting QCM-modified electrodes were imaged in air using a Molecular Imaging PicoLe AFM in tapping mode and silicon cantilevers (Nanosensors) with a resonance frequency of 200–400 kHz. Topographic, amplitude, and phase images were recorded for all modified substrates with a resolution of 512×512 pixels. AFM measurements were carried out for freshly modified substrates and repeated after several days of drying at room temperature. From the tapping mode AFM images, the type of surface bonding of the rods and their surface density were determined.

2.7. Contact Angle Measurements. The wetting properties of the QCM electrodes upon consecutive self-assembly of 1,6HDT and AuNRs were determined by contact angle measurements using a homemade goniometer, and 5 μL ultrapure Millipore water drops which were gently deposited on the modified substrates by keeping the micropipet perpendicular to the surface. All the contact angle measurements were performed five times for each layer, depositing the water drops on different spots of the modified QCM electrodes, at room temperature. The images obtained were analyzed using Image J software.

2.8. Fourier Transform Infrared Reflection–Absorption Spectroscopy Measurements. The covalent bonding of the AuNRs to the Au-1,6HDT-SAM modified electrode was verified by FT-IRRAS measurements using a Bruker PM-FT-IRRAS spectrophotometer (LN-MCT-Narrow, PMA50 detector, cooled

with liquid nitrogen). Commercial gold slides were carefully cleaned by washing with ethanol, acetone, and Millipore water, dried in a stream of nitrogen, and consecutively modified following the procedure described above. After their modification, the Au-1,6HDT-SAM, Au-1,6HDT-AuNR₁, and Au-1,6HDT-AuNR₂ modified slides were washed with Millipore water and ethanol, consecutively, dried in a stream of nitrogen, and analyzed by PM-FT-IRRAS spectroscopy (Figure 4). For comparison, attenuated total reflectance infrared spectra of cetyltrimethyl ammonium bromide (5 mg) powder and liquid 1,6-hexanedithiol (3 μ L) incorporated in KBr were measured in air using the internal detector of the spectrophotometer (Bruker, Tensor 27) (Figure 3).

2.9. Electrochemical Measurements. Cyclic, square wave voltammetry, and electrochemical impedance spectroscopy measurements were performed on a PGSTAT 302N potentiostat (EcoChemie B.V., The Netherlands). All electrochemical experiments were carried out in a conventional three-electrode cell equipped with a working electrode of gold (0.0314 cm² area), a Pt wire as the counter electrode, and a Ag/AgCl (3 M KCl) electrode as the reference electrode. The gold electrodes were cleaned as explained elsewhere²⁴ and modified by immersion in a 0.015 M ethanolic solution of 1,6-hexanedithiol at 25 °C for 14 h, followed by washing with ethanol and Millipore water, and dried in a stream of nitrogen. Electrochemical measurements were performed for the Au-1,6HDT-SAM modified electrode in an aqueous solution of 0.1 M NaClO₄ (supporting electrolyte) and 0.0005 M [Fe(CN)₆]^{3-/4-} redox probes. Consecutively, freshly cleaned gold electrodes were modified by immersion in a 0.015 M ethanolic solution of 1,6-hexanedithiol at 25 °C for 14 h, followed by washing with ethanol and Millipore water, drying in a stream of nitrogen, and immersion in a 0.50 mg/mL aqueous solution of AuNR₁ at 35 °C for 5 h. The resulting Au-1,6HDT-AuNR₁ modified electrode was washed with Millipore water and tested electrochemically using 0.1 M NaClO₄ and 0.0005 M [Fe(CN)₆]^{3-/4-} aqueous solutions. The same procedure was used for 7, 15, and 24 h immersion times of Au-1,6HDT-SAM in an aqueous solution of AuNR₁. Similarly, Au-1,6HDT-AuNR₂ modified electrodes were fabricated by immersion of Au-1,6HDT-SAM electrodes in a 0.50 mg/mL aqueous solution of AuNR₂, at 35 °C for 5, 15, and 24 h. The resulting Au-1,6HDT-AuNR₂ modified electrodes were washed with Millipore water and tested electrochemically. Cyclic voltammograms were recorded for various scan rates: 25, 50, 75, and 100 mV/s within the potential window of 0.2–0.6 V. Square wave voltammograms were measured for the same potential window, at frequencies varying between 10 and 75 Hz, using a 50 mV amplitude and a step potential of 2 mV. Electrochemical impedance spectroscopy (EIS) measurements were performed for a frequency range of 40 000–0.1 Hz, with amplitude of 20 mV and at the midpeak potentials determined from the CVs. For deaeration, gaseous nitrogen was purged in the 0.1 M NaClO₄/0.0005 M [Fe(CN)₆]^{3-/4-} aqueous solution before each measurement.

3. Results

3.1. Characterization of the AuNRs. The UV–vis spectra measured for the synthesized gold nanorods are presented in Figure S1 (Supporting Information). The gold nanorods showed transverse plasmon bands at 517 nm (AuNR₁) and 515 nm (AuNR₂) and longitudinal plasmon bands at 650 nm (AuNR₁) and 749 nm (AuNR₂). Transmission electron microscopy and size distribution measurements presented in Figure S2 (Supporting Information) show that the aspect ratios of the gold nanorods were 2.33 \pm 0.05 (a) (AuNR₁, average length per

width of 38.20 \pm 0.72 nm per 16.40 \pm 0.23 nm) and 3.16 \pm 0.02 (AuNR₂, average length per width of 50 \pm 0.48 nm per 15.82 \pm 0.08 nm).

3.2. Characterization of Au-1,6HDT-AuNR Modified Electrodes.
3.2.1. Quartz Crystal Microbalance (QCM) and Atomic Force Microscopy (AFM) Measurements. The quartz crystal microbalance is an ultrasensitive weighing device in which an ac voltage is pulsed across a piezoelectric AT-quartz crystal at the crystal's resonant frequency ($n = 1, 5$ MHz) and at several overtones, causing the crystal to oscillate in shear mode at each frequency. The change in the resonant or overtone frequency of the crystal, ΔF , is proportional with the change in mass per unit area, Δm , of any film adsorbed to the crystal surface²⁶

$$\Delta m = -\frac{C}{n}\Delta F \quad (1)$$

where C is a constant that depends on the physical properties of the quartz crystal ($C = 18.0$ ng/cm² Hz for the quartz crystal used in this work) and n is the overtone number ($n = 1, 3, 5, \dots$). Moreover, the surface coverage can be calculated using eq 2

$$\Gamma = \frac{\Delta m}{FW} \quad (2)$$

where Γ is in units of mol/cm² and FW is the formula weight of the adsorbed species.

Using QCM measurements, we have determined the kinetics of the 1,6HDT and AuNR self-assembly process. The first layer self-assembled on QCM electrodes, the 1,6HDT monolayer, was formed on the gold quartz crystal electrodes over a period of 14 h, having a mass of $(0.23 \pm 0.05) \times 10^{-5}$ g/cm² (Supporting Information, Figure S3b), which corresponds to a frequency decrease of $\Delta F = -125.60 \pm 31.78$ Hz (Supporting Information, Figure S3a) and a surface coverage of 0.0015×10^{-5} mol/cm² (equivalent to 9.20×10^{15} molecules/cm²), as determined from the frequency and mass change measurements (Supporting Information, Figure S3) and using eq 2. The thickness of the 1,6HDT monolayer was 33.0 \pm 1.70 nm, which is consistent with previous QCM characterizations of this monolayer.^{27,28} For each bilayer built on the QCM electrodes, the 1,6HDT-SAM showed a similar mass deposition. The frequency change recorded during the 1,6HDT self-assembly from ethanolic solution, at 25 °C (Supporting Information, Figure S3a), showed a continuous decrease, indicating a continuous chemisorption of the 1,6HDT to the gold substrates, being faster initially (sharper ΔF decrease in the first 6 h), slower for the following hours due to the rearrangement of the 1,6HDT molecules, and stabilizing at the end of the 14 h time of self-assembly. Consecutively, the gold nanorods were self-assembled onto Au-1,6HDT-SAM modified electrodes by injection of AuNR solutions (0.50 mg/mL) into the QCM chamber at 35 °C. It was observed that, at this solution temperature, 2.33 aspect ratio rods needed 5 h of chemisorption, whereas 3.16 aspect ratio rods needed 11 h of chemisorption in order to form stable three-dimensional bilayers (Figure 1) onto Au-1,6HDT-SAM modified electrodes. Moreover, both types of rods were vertically attached (bonded at their tips) to the modified substrates with a high surface coverage, as proven by tapping mode AFM images (Figure 1; see Table 1). The recorded frequency decrease was $\Delta F = -74.32 \pm 8.0$ Hz during the chemisorption of 2.33 aspect ratio rods (Supporting Information, Figure S3c) and $-288 \pm$

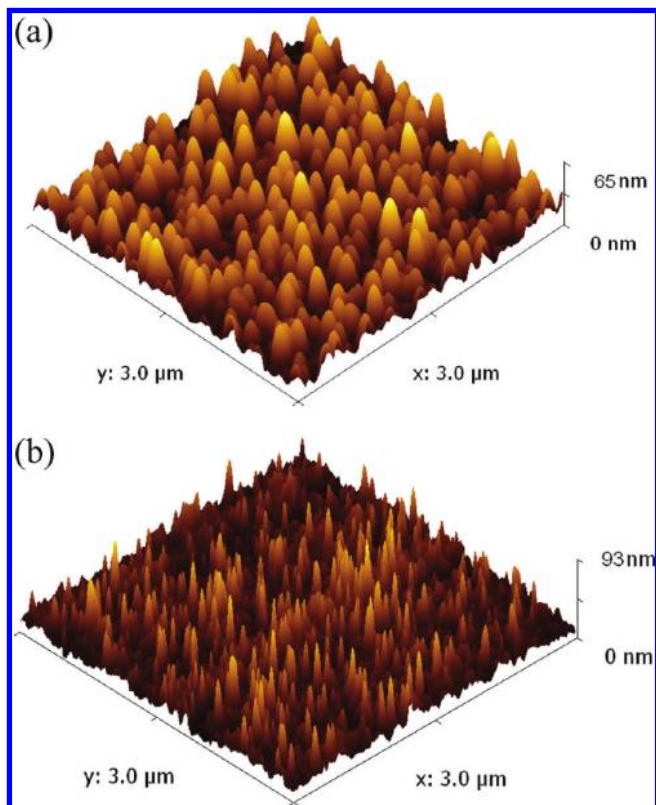


Figure 1. 3D topographic tapping mode AFM images of gold nanorods with aspect ratios of 2.33 (a) and 3.16 (b) chemisorpt onto 1,6-hexanedithiol-modified gold substrates at a solution temperature of 35 °C. The chemisorption time was 7 (a) and 15 h (b). The size of the images was 3 $\mu\text{m}/3 \mu\text{m}$.

TABLE 1: Root-Mean-Square Roughness Corresponding to the Topographic Tapping Mode AFM Images Represented in Figure 1

surface	rms (nm)	figure
bare gold	1.83	
1,6HDT layer	1.21	
1,6HDT-AuNR ₁ bilayer	11.24	1a
1,6HDT-AuNR ₂ bilayer	14.23	1b

53 Hz during the chemisorption of 3.16 aspect ratio rods (Supporting Information, Figure S3e) to Au-1,6HDT-SAM modified electrodes. These frequency decreases correspond to mass depositions of $(0.14 \pm 0.01) \times 10^{-5}$ g (AuNR₁) and $(0.53 \pm 0.15) \times 10^{-5}$ g (AuNR₂), respectively (Supporting Information, Figure S3d,f). The average surface coverage was 1.78×10^9 AuNR₁/cm² and 2.80×10^9 AuNR₂/cm², as determined from the AFM images (Figure 1). As represented in Figure S3c,d (Supporting Information), during the AuNR₁ self-assembly process, the decrease of frequency is sharp and continuous, while the mass deposited follows the same trend, but in opposite direction (sharp and continuous increase), proving that the attachment of 38.20 nm/16.40 nm gold nanorods is a fast and continuous process. The curve of frequency showed the same features, even after a 24 h time of AuNR₁ self-assembly (results not shown). Interestingly, AFM imaging revealed an almost complete coverage of the QCM electrodes with 2.33 aspect ratio rods after 24 h of chemisorption and the formation of vertically packed rod assemblies with significant interaction or even contact between adjacent individual AuNR₁ (see Figure S4 in the Supporting Information). Similar kinetics were observed during the self-assembly of 14 nm citrate-stabilized Au NPs within redox multilayers.²⁹ Concerning the longer rods, their

self-assembly process proved to be faster during the first 8 h (sharp Δf decrease, sharp Δm increase, Supporting Information, Figure S3e,f), followed by a slower self-assembly process until stabilization (11 h). A longer adsorption time for the 3.16 aspect ratio rods resulted in a low increase of surface coverage. These results suggest that the size of the gold nanorods has an important effect on the kinetics of their chemisorption onto Au-1,6HDT-SAM modified electrodes. Smaller rods seem to have an increased freedom to attach to the -SH groups of the 1,6HDT monolayer than the longer rods. AFM imaging revealed that the drying of the Au-1,6HDT-AuNR modified QCM electrodes has an important effect on the bilayers' topography. In a typical top view of the tapping mode AFM images (Supporting Information, Figure S5a), the vertically aligned gold nanorods appear as spherical nanoparticles due to the fact that what we see are the tips of the rods. This is specific for freshly prepared samples. Drying the Au-1,6HDT-AuNR modified QCM electrodes for 5 days resulted in a tilted arrangement of the rods on the substrates (Supporting Information, Figure S5b). In our previous paper, we have shown that the chemisorption of the AuNRs onto Au-1,6HDT-SAM modified electrodes at a 27 °C solution temperature yields a low surface coverage with rods.²⁴ In consequence, the Au-1,6HDT-AuNR modified electrodes showed a low recovery of the electronic communication between the electroactive species in solution and the underlying gold electrodes.²⁴ In the present work, the increase of temperature during the self-assembly process of the rods has three important effects: (i) it decreases the time of rods' chemisorption, (ii) it increases the density of the rods on the substrates, and (iii) it changes the surface bonding type of the longer rods from side surface bonding to end surface bonding. This may be due to the fact that the CTAB stabilizing the rods is completely soluble in water at 35 °C and is less dense at the ends (tips) of the rods than at their sides,³⁰ facilitating in a higher degree the formation of Au-S-C bonds at the tips of the gold nanorods. An increased density of the rods self-assembled on Au-1,6HDT-SAM modified electrodes will have an important influence on their electrochemical properties, as it will be discussed in the following paragraphs.

In previous published papers, the electrochemical properties of NP-modified electrodes were mainly studied as a function of the number of layers, nanoparticles size, or surface density using various electroactive species.^{2,8,16–18} In most cases, the surface density of the nanoparticles self-assembled on modified electrodes was increased by allowing a longer time of adsorption of NPs from solution to the electrodes' surface. In our work, the surface density of the AuNRs is increased by increasing their solution temperature during the adsorption process. This leads to a decrease of their self-assembly time and generates vertically aligned AuNR assemblies. In consequence, the electrochemical properties of Au-1,6HDT-AuNR modified electrodes will be influenced by the size, surface density, and surface alignment of the rods. Because the rods are vertically attached to the Au-1,6HDT-SAM modified electrodes (Figure 1 and Figures S4 and S5 in the Supporting Information), it is reasonable to consider that the thickness of these bilayers is determined by the thickness of the 1,6HDT monolayer and the length of the gold nanorods (38.20 nm for AuNR₁ and 50 nm for AuNR₂, as determined from TEM images, Supporting Information, Figure S2). The average thickness of the 1,6HDT-AuNR₁ bilayer was 69.23 ± 3.39 nm, whereas the average thickness of the 1,6HDT-AuNR₂ was 81 ± 2.62 nm for freshly prepared bilayers.

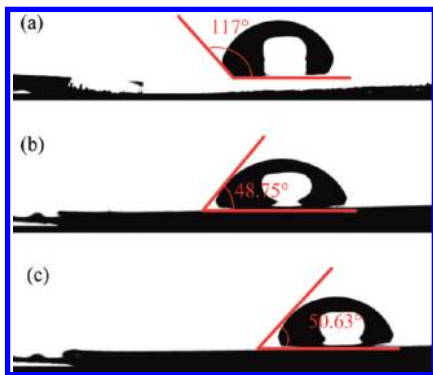


Figure 2. Contact angle images of 5 μL Millipore water drops deposited onto (a) Au-1,6HDT, (b) Au-1,6HDT-AuNR₁, and (c) Au-1,6HDT-AuNR₂ modified electrodes. Images were recorded at 25 $^{\circ}\text{C}$ room temperature. The self-assembly times were 7 h for AuNR₁ (2.33 aspect ratio) and 15 h for AuNR₂ (3.16 aspect ratio).

3.2.2. Contact Angle and Fourier Transform Infrared Reflection–Absorption Spectroscopy Measurements. The presence of each layer self-assembled on Au electrodes was confirmed by contact angle and FT-IRRAS spectroscopy measurements. The contact angle, θ , is a quantitative measure of the wetting of a solid substrate by a liquid. It is well-known that low values of the contact angle ($\theta < 90^{\circ}$) indicate that the liquid spreads or wets the modified substrates well (the layer on the substrate has hydrophilic properties), whereas high values ($\theta > 90^{\circ}$) indicate poor wetting (the layer on the substrate has hydrophobic properties).³¹ The 1,6HDT monolayer self-assembled on Au electrodes proved to have hydrophobic features when covered by water drops, with a contact angle of $\theta = 117^{\circ}$ (Figure 2a). Contrarily, the AuNR layers self-assembled on Au-1,6HDT-SAM modified electrodes showed hydrophilic properties with contact angles of $\theta = 48.75^{\circ}$ (AuNR₁, Figure 2b) and $\theta = 50.63^{\circ}$ (AuNR₂, Figure 2c). This is consistent with the physical properties of 1,6-hexanedithiol, which is not soluble in water, whereas cetyltrimethyl ammonium bromide (CTAB), stabilizing the rods, is partially soluble in water at room temperature. The variations of the contact angle parameter prove that the 1,6HDT-SAM and AuNRs were covering the Au electrodes quite uniformly, as presented also in the AFM images (Figure 2 and Figures S4 and S5 in the Supporting Information).

When the ATR-FTIR spectrum of cetyltrimethyl ammonium bromide powder (Figure 3a) was analyzed, the following vibrations bands were identified: symmetric $\nu\text{C-H}$ stretching vibration band at 2850 cm^{-1} and asymmetric $\nu\text{C-H}$ stretching vibration band at 2918 cm^{-1} of the aliphatic $-\text{CH}_2-$ groups, scissor deformation of $-\text{CH}_2-$ groups at 1463 cm^{-1} , and rocking deformation of $-\text{CH}_2-$ and $-\text{CH}_3$ at 717 cm^{-1} .³⁰ The strong peaks at 910 and 964 cm^{-1} correspond to the C–N stretching vibration in an aliphatic amine (between 1300 and 900 cm^{-1}), whereas the weak peaks at 1410 and 1244 cm^{-1} correspond to the C–N bending vibration. Moreover, the absence of a strong stretching vibration band specific for a N–H bond at 3300 cm^{-1} confirms the presence of a quaternary amine.³²

The 1,6HDT molecule generated the following absorption bands in the ATR-FTIR spectrum: $\nu\text{C-H}$ symmetric and asymmetric stretching vibration of the $-\text{CH}_2-$ groups at 2850 and 2923 cm^{-1} and a band with a broad peak due to the S–H stretching vibration at 2678 cm^{-1} (Figure 3b). In the fingerprint region, scissor deformation of the $-\text{CH}_2-$ groups at 1458 cm^{-1} , twisting deformation of the $-\text{CH}_2-$ groups at 1272 cm^{-1} , rocking vibration of the $-\text{CH}_2-$ groups at 730 cm^{-1} , and

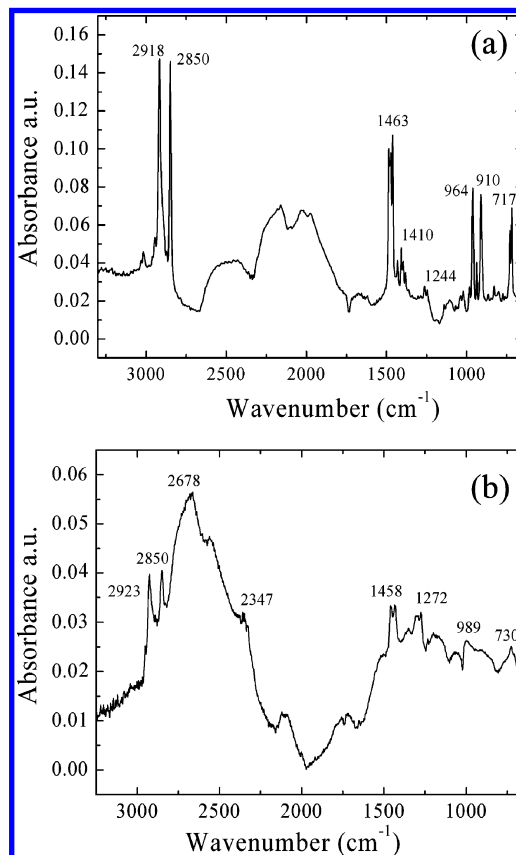


Figure 3. ATR-FTIR spectra of cetyltrimethyl ammonium bromide (a) and 1,6-hexanedithiol (b).

bending vibration of the S–H group at 989 cm^{-1} were observed.³² When self-assembled on gold electrodes, the spectrum of the 1,6HDT showed vibration bands at 2852, 2925, and 2962 cm^{-1} due to the $\nu\text{C-H}$ symmetric and asymmetric stretching vibration of the $-\text{CH}_2-$ groups, together with a peak at 2626 cm^{-1} due to the S–H stretching vibration (Figure 4a). In the fingerprint region of the spectrum were observed scissoring vibrations of the C–H bonds of the $-\text{CH}_2-$ groups at 1457 and 1538 cm^{-1} , twisting deformation of $-\text{CH}_2-$ groups at 1261 cm^{-1} , bending vibration of the S–H group at 1087 and 1093 cm^{-1} , and rocking vibration of the $-\text{CH}_2-$ groups at 798 cm^{-1} (Figure 4b). The vibration bands observed in the FT-IRRAS spectrum prove that the 1,6HDT monolayer is attached to the Au electrodes through one $-\text{S-H}$ group of the dithiol, the second $-\text{S-H}$ group being free and available for further chemical interactions (e.g., covalent bonding to the AuNR tips). The FT-IRRAS spectra of the Au-1,6HDT-AuNR₁ and Au-1,6HDT-AuNR₂ modified substrates, extracted from PM-IRRAS interferograms, are represented in Figure 4c,d. The vibration bands identified in these spectra revealed interesting details about the chemical structure of the bilayers. The spectra of the 1,6HDT-AuNR bilayers were mainly similar to the ATR-FTIR spectrum of CTAB. Both bilayers showed well-defined $\nu\text{C-H}$ symmetric and asymmetric stretching vibration of the $-\text{CH}_2-$ groups at 2848 and 2916 cm^{-1} (1,6HDT-AuNR₁ bilayer, Figure 4c, black line) or 2848 and 2920 cm^{-1} (1,6HDT-AuNR₂ bilayer, Figure 4c, red line). We could expect that, by covalent bonding of the AuNRs to the 1,6HDT monolayer, the stretching vibration band of free $-\text{S-H}$ groups will disappear. As seen by AFM imaging (Figure 1 and Figure S5 in the Supporting Information) after 7 (AuNR₁) or 15 h (AuNR₂) of chemisorption, the rods do not cover completely the Au-1,6HDT-SAM modified substrate. This explains the presence of a weak band at 2644 cm^{-1}

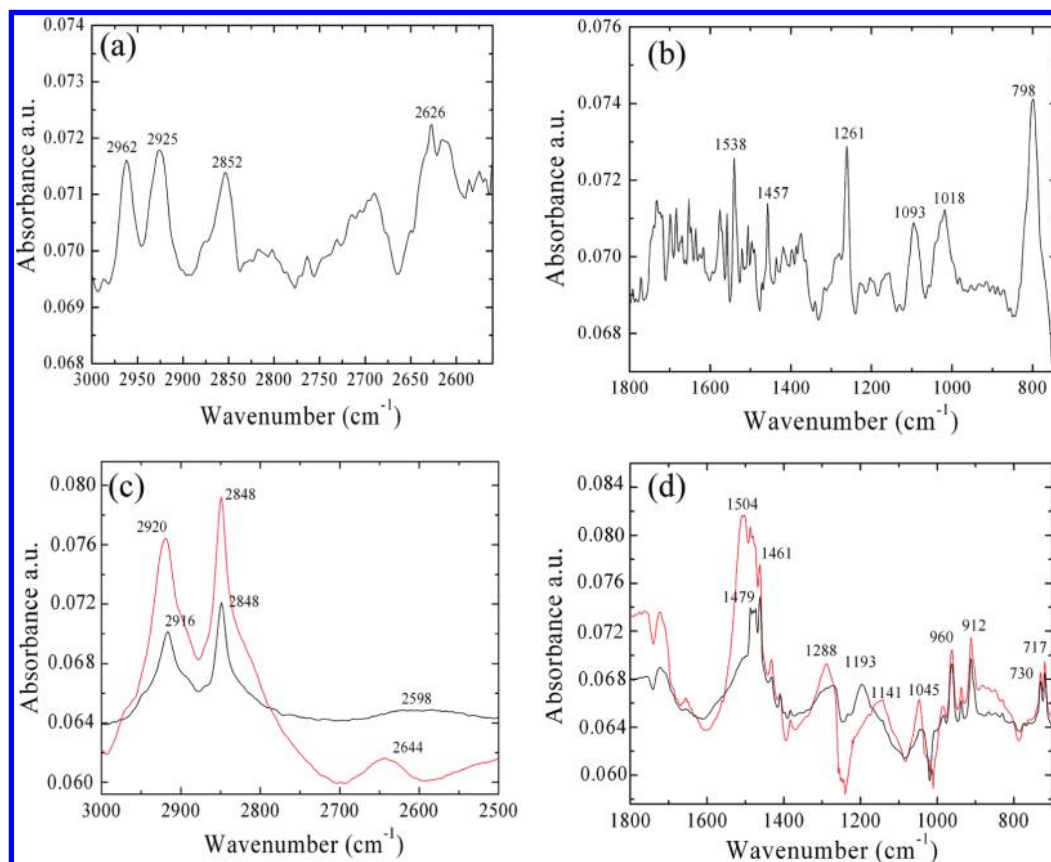


Figure 4. FT-IRRAS spectra of 1,6-hexanedithiol self-assembled on gold substrates (a, b) and 2.33 aspect ratio rods (black line) or 3.16 aspect ratio rods (red line) self-assembled onto Au-1,6HDT-SAM modified Au substrates (c, d).

(Figure 4c, red line) or 2598 cm^{-1} (Figure 4c, black line) due to the —S—H stretching vibration, which means there still exists a small amount of free —S—H groups of the 1,6HDT-SAM under the AuNR layers. After a 24 h self-assembly time, this weak band in the FT-IRRAS spectra of Au-1,6HDT-AuNR₁ modified electrodes disappeared completely due to an almost complete surface coverage with AuNR₁, for example (results not shown). In the fingerprint region of the FT-IRRAS spectra, both bilayers showed strong peaks at 912 and 960 cm^{-1} due to C—N stretching vibration and weak peaks at 1045 and 1193 cm^{-1} (AuNR₁ layer, black line, Figure 4d) or 1141 and 1045 cm^{-1} (AuNR₂ layer, red line, Figure 4d) due to the C—N bending vibration (between 1200 and 1020 cm^{-1}).³² The vibration band at 1288 cm^{-1} is due to the twisting deformation of the $\text{—CH}_2\text{—}$ groups, whereas the vibration band at 1479 cm^{-1} (AuNR₁ layer, black line, Figure 4d) or 1461 cm^{-1} (AuNR₂ layer, red line, Figure 4d) is due to scissor deformation of the $\text{—CH}_2\text{—}$ groups in the aliphatic chain of the CTAB stabilizing the AuNRs. The vibration bands at 717 and 730 cm^{-1} are due to rocking deformations of the C—H bonds in the $\text{—CH}_2\text{—}$ and CH_3 groups. There is no identifiable band for the 1,6HDT molecule in the fingerprint region of the bilayers (S—H bending, for example), but this band could be masked by C—N bending vibrations. Also, the 1,6HDT monolayer could have a contribution through the $\text{—CH}_2\text{—}$ vibration bands observed in the FT-IRRAS spectra of the bilayers. Overall, the FT-IRRAS spectra of the Au-1,6HDT-AuNR modified electrodes prove that the AuNRs were covalently bonded to the 1,6HDT self-assembled monolayer.

3.2.3. Cyclic Voltammetry, Square Wave Voltammetry, and Electrochemical Impedance Spectroscopy Measurements. The electrochemical properties of Au-1,6HDT-AuNR₁ and Au-

1,6HDT-AuNR₂ modified electrodes as a function of the adsorption time of the AuNRs were studied by cyclic voltammetry, square wave voltammetry, and electrochemical impedance spectroscopy. For these experiments, $n = 0$ corresponds to the bare gold electrode, $n = 1$ corresponds to the Au-1,6HDT-SAM modified electrode, and $n = 2a_1, 2a_2, 2a_3$, and $2a_4$ corresponds to 5, 7, 15, and 24 h immersion times of Au-1,6HDT-SAM modified electrodes in a 0.50 mg/mL AuNR₁ aqueous solution (2.33 aspect ratio rods) at 35°C . Similarly, $n = 2b_1, 2b_2$, and $2b_3$ corresponds to 5, 15, and 24 h immersion time of Au-1,6HDT-SAM modified electrodes in a 0.50 mg/mL AuNR₂ aqueous solution (3.16 aspect ratio rods) at 35°C . Evidently, the adsorption time of AuNRs (self-assembly time) is equal to the immersion time of the Au-1,6HDT-SAM modified electrodes in AuNR solutions. As proven by AFM imaging and FT-IRRAS spectroscopy measurements (Figures 1–4), the AuNRs were covalently attached to the Au-1,6HDT-SAM modified electrodes in an end-bonding topography and with a high surface density.

Figures 5 and 6 represent the cyclic voltammograms and the square wave voltammograms recorded at the bare electrode ($n = 0$), Au-1,6HDT-SAM modified electrode ($n = 1$), Au-1,6HDT-AuNR₁ ($n = 2a_1\text{--}4$, Figure 5), and Au-1,6HDT-AuNR₂ modified electrodes ($n = 2b_1\text{--}3$, Figure 6) in an aqueous solution containing 0.1 M NaClO_4 as the supporting electrolyte and $0.0005\text{ M [Fe(CN)}_6\text{]}^{3-/4-}$ as the redox probe. As seen previously, the 1,6-hexanedithiol has an insulating effect when self-assembled on gold electrodes.^{24,33,35} This is proven by the disappearance of the Faradaic current at the Au-1,6HDT-SAM modified electrode (Figure 5, $n = 1$) as compared with the bare gold (Figure 5, $n = 0$), confirming a dense packing of the 1,6HDT molecules on the Au electrode surface. In other words,

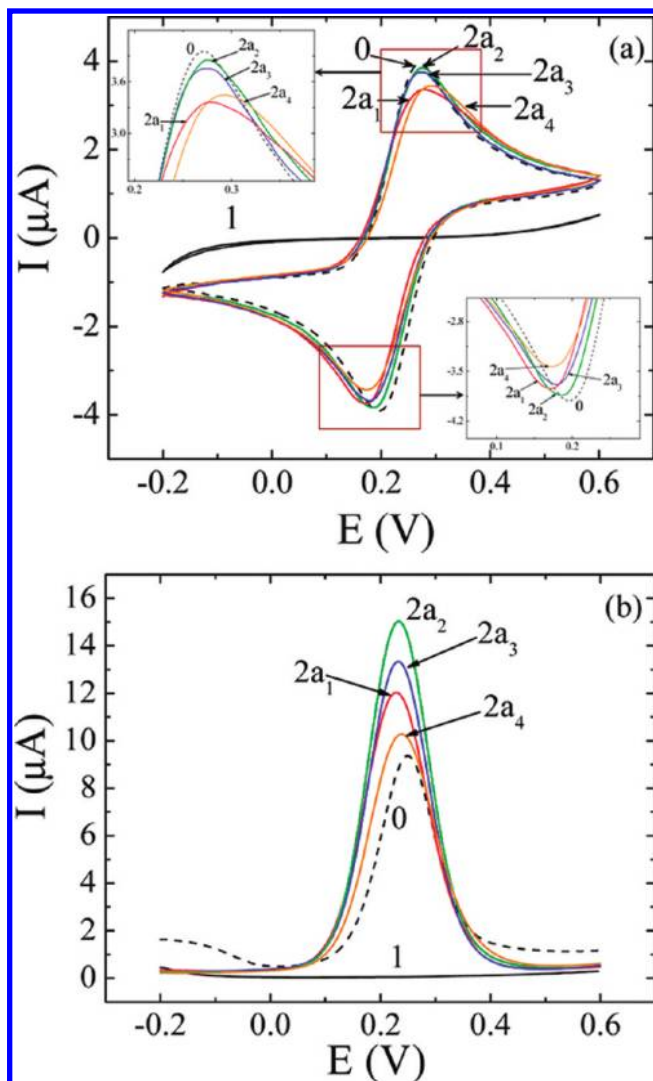


Figure 5. (a) Cyclic voltammograms recorded at the modified electrodes in an aqueous 0.1 M NaClO₄ solution containing 0.0005 M [Fe(CN)₆]^{3−} and 0.0005 M [Fe(CN)₆]^{4−}: bare gold ($n = 0$), Au-1,6HDT-SAM ($n = 1$), and Au-1,6HDT-AuNR₁ modified electrodes for 5 h ($n = 2a_1$, red line), 7 h ($n = 2a_2$, green line), 15 h ($n = 2a_3$, blue line), and 24 h of chemisorption of AuNR₁ ($n = 2a_4$, orange line). Scan rate: 50 mV/s. (b) Square wave voltammograms of the modified electrodes recorded in the same conditions. Frequency scan: 10 Hz. The average length/width of the rods was 38.20 nm/16.40 nm.

the 1,6HDT-SAM is blocking the electronic communication between [Fe(CN)₆]^{3−/4−} in solution and the underlying gold electrode surface. This electrochemical behavior is also sustained by contact angle measurements that showed that this layer has hydrophobic properties (Figure 2a). In consequence, the diffusion of the electroactive species through this layer is highly hindered. Also, the diffusion of the supporting electrolyte (0.1 M NaClO₄) through the 1,6HDT monolayer was highly hindered, as proven by cyclic voltammetry measurements (Supporting Information, Figure S6a). The NaClO₄ showed no evident effect on the bilayers' structure during the electrochemical measurements (Supporting Information, Figure S6b).

The successive self-assembly of AuNRs onto Au-1,6HDT-SAM modified electrodes switched on an efficient path for electron transfer from the [Fe(CN)₆]^{3−/4−} redox probe in solution toward the underlying Au electrode surface. Cyclic voltammograms with high peak currents and decreased peak separation were recorded at both Au-1,6HDT-AuNR modified electrodes (Figures 5a and 6a). Depending on the immersion time of Au-

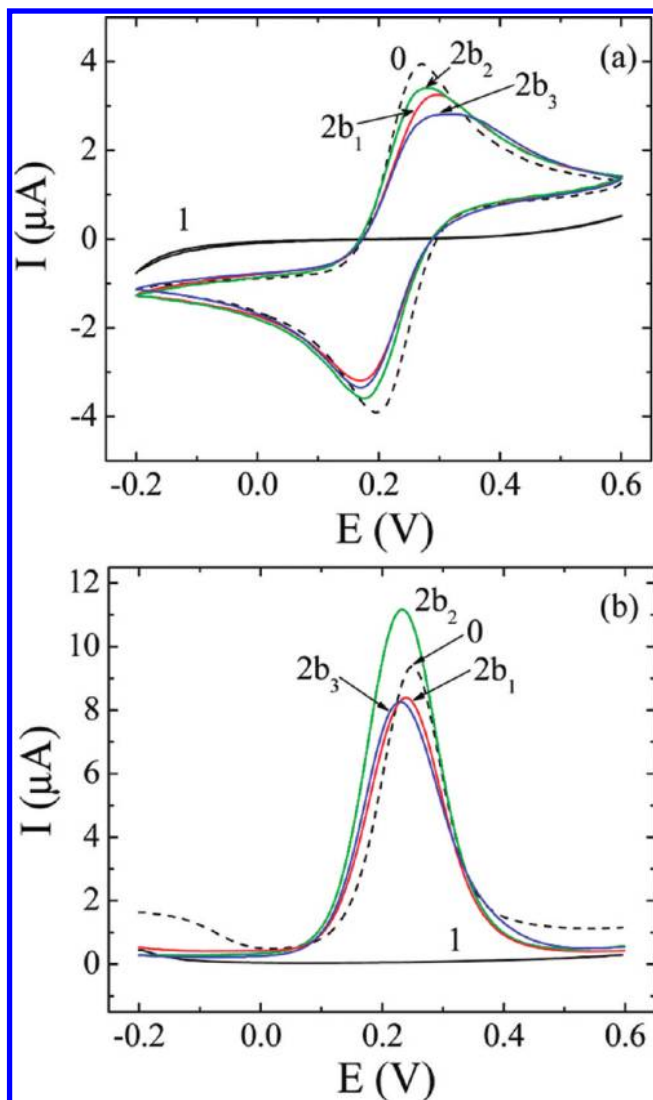


Figure 6. (a) Cyclic voltammograms recorded at the modified electrodes in an aqueous 0.1 M NaClO₄ solution containing 0.0005 M [Fe(CN)₆]^{3−} and 0.0005 M [Fe(CN)₆]^{4−}: bare gold ($n = 0$), Au-1,6HDT-SAM ($n = 1$), and Au-1,6HDT-AuNR₂ modified electrodes for 5 h ($n = 2b_1$, red line), 15 h ($n = 2b_2$, green line), and 24 h of chemisorption of AuNR₂ ($n = 2b_3$, blue line). Scan rate: 50 mV/s. (b) Square wave voltammograms of the modified electrodes recorded in the same conditions. Frequency scan: 10 Hz. The average length/width of the rods was 50 nm/15.82 nm.

1,6HDT-SAM modified electrodes in an aqueous solution of AuNRs, the peak currents in the CVs recorded at Au-1,6HDT-AuNR modified electrodes increased with the immersion time but started to decrease after 24 h. The highest enhancement of the electrical current in the cyclic voltammograms was recorded after 7 h of chemisorption of AuNR₁ ($n = 2a_2$, Figure 5a) or 15 h of chemisorption of AuNR₂ ($n = 2b_2$, Figure 6a) onto Au-1,6HDT-SAM electrodes. This represents the optimum time of AuNR self-assembly onto Au-1,6HDT-SAM modified electrodes in order to reach a maximum improvement of the electrochemistry of [Fe(CN)₆]^{3−/4−} probes at the modified electrodes.

In the square wave voltammograms was observed a similar electrochemical behavior (Figures 5b and 6b). At the optimal time of AuNR chemisorption, the square wave voltammograms recorded at the Au-1,6HDT-AuNR modified electrodes in aqueous 0.1 M NaClO₄ and 0.0005 M [Fe(CN)₆]^{3−/4−} showed higher peak currents than those at the bare gold electrode. This is due to the higher sensitivity of square wave voltammetry

toward surface confined electron-transfer processes than cyclic voltammetry.^{16,17} At the Au-1,6HDT-AuNR₁ electrodes, the peak-to-peak separations in the CVs varied as follows: 0.105 V for $n = 2a_1$ (5 h), 0.088 V for $n = 2a_2$ (7 h), 0.094 V for $n = 2a_3$ (15 h), and 0.117 V for $n = 2a_4$ (24 h) as compared to bare gold 0.076 V ($n = 0$) (Figure 5a). At the Au-1,6HDT-AuNR₂ electrodes, the peak-to-peak separations in the CVs varied as follows: 0.124 V for $n = 2b_1$ (5 h), 0.101 V for $n = 2b_2$ (15 h), and 0.140 V for $n = 2b_3$ (24 h) (Figure 6a). The corresponding peak currents and shifting of the peak potentials in the SQWVs were 9.36 μ A and 0.249 V for $n = 0$ (bare gold), 12.03 μ A and 230 mV for $n = 2a_1$ (5 h), 15.08 μ A and 232 mV for $n = 2a_2$ (7 h), 13.33 μ A and 233 mV for $n = 2a_3$ (15 h), 10.28 μ A and 238 mV for $n = 2a_4$ (24 h), 8.45 μ A and 0.238 V for $n = 2b_1$ (5 h), 11.16 μ A and 0.232 V for $n = 2b_2$ (15 h), and 8.23 μ A and 0.230 V for $n = 2a_3$ (24 h), respectively, (Figures 5b and 6b). Because the electroactive species in solution are negatively charged and the CTAB, stabilizing the rods, is positively charged, it is reasonable to expect an electrostatic attraction between $[\text{Fe}(\text{CN})_6]^{3-/4-}$ in solution and the AuNRs at the Au-1,6HDT-AuNR/solution interface.^{2,16,17} Additionally, the AuNR layers are hydrophilic (Figure 2b,c), and in consequence, the diffusion of the electroactive species through these layers is highly favored. This means that the concentration of $[\text{Fe}(\text{CN})_6]^{3-/4-}$ redox probes at the Au-1,6HDT-AuNR/solution interface is increased by electrostatic attraction and the charging of the rods by the electroactive species in solution is highly favored. To this assumption is contributing also the fact that the 1,6HDT monolayer under the AuNR layer is hydrophobic and acts as barrier against ion and molecule diffusion. Because of the insulating properties (Figures 5 and 6, $n = 1$) and hydrophobic nature of the 1,6HDT monolayer (Figure 2a), the electron transfer through this layer will take place by through-bond tunneling^{24,33,35,36} because the diffusion of the redox probes is highly hindered by this layer. The cumulative effects of the two layers self-assembled on gold electrodes suggest that the electrochemical process of $[\text{Fe}(\text{CN})_6]^{3-/4-}$ probes at Au-1,6HDT-AuNRs is a three-step process: electron charging of the nanorods from the electroactive species in solution, electron transport through the nanorods, and a coherent electron tunneling across the 1,6HDT monolayer toward the underlying Au electrode (Scheme 1). A similar electrochemical behavior was observed for single-walled or multiwalled carbon nanotubes attached to Au electrodes through alkanethiol SAM.^{33,34}

When an insulating barrier exists, the redox current at any potential will decrease with the thickness of the insulating film according to the expression³⁴

$$I = I_0 e^{-\beta d} \quad (3)$$

where I_0 is the current measured at the bare electrode, β is the potential-independent electron tunneling coefficient, and d is the thickness of the monolayer. For an electrochemical reaction at equilibrium, using eq 1, it can be obtained

$$k = k_0 e^{-\beta d} \quad (4)$$

where k_0 and k are the electron-transfer rate constants at the bare and 1,6HDT-SAM modified electrode. The heterogeneous electron-transfer rate constant (k_{et}) at the modified electrodes can be calculated using eq 5¹⁸

$$k_{\text{et}} = \frac{RT}{n^2 F^2 A R_{\text{CT}} c^0} \quad (5)$$

where R is the gas constant, T is temperature (K), F is the Faraday constant, A is the electrode area (cm^2), R_{CT} is the charge-transfer resistance, c^0 is the concentration of the redox couple in the bulk solution ($0.50 \times 10^{-3} \text{ mol/cm}^3$), and n is the number of transferred electrons per molecule of the redox probe ($n = 1$ for the $[\text{Fe}(\text{CN})_6]^{3-/4-}$ probes). The apparent charge-transfer resistance values were obtained from fittings of the EIS spectra and used to estimate the heterogeneous electron-transfer rate constants, k_{et} . Upon AuNR adsorption to the Au-1,6HDT-SAM modified electrodes, the k_{et} value increased 3 orders of magnitude, proving the activation of an efficient path for electron transfer. The variation of the heterogeneous electron-transfer rate constant, k_{et} , showed that the electron-transfer process was dependent on the density of the rods on the substrates (Table 2). When 38.20 nm/16.40 nm rods were self-assembled to the modified substrates from 5 to 7 h, the heterogeneous electron-transfer rate constant increased slightly from $(1.51 \pm 0.02) \times 10^{-5} \text{ cm} \times \text{s}^{-1}$ to $(1.58 \pm 0.03) \times 10^{-5} \text{ cm} \times \text{s}^{-1}$ (highest value of k_{et}). For longer chemisorption times (15–24 h), the k_{et} decreased to half of the highest estimated value. When 50 nm/15.82 nm rods were adsorbed to the modified substrates from 5 to 15 h, the heterogeneous electron-transfer rate constant increased from $(0.72 \pm 0.02) \times 10^{-5} \text{ cm} \times \text{s}^{-1}$ to $(1.00 \pm 0.05) \times 10^{-5} \text{ cm} \times \text{s}^{-1}$, followed by a sharper decrease for 24 h of chemisorption time (Table 2). These variations of k_{et} confirms the fact that the fastest electron-transfer process takes place at Au-1,6HDT-AuNR₁ modified electrodes for an optimal time of 7 h of chemisorption of AuNR₁ onto Au-1,6HDT-SAM modified electrodes. Although the 1,6HDT-SAM is 30° tilted to the normal surface, the thickness of the insulating barrier is represented by the 1,6HDT length (8 units \times 1.25 Å), which is the same for both bilayers. The electron tunneling process will take place through the entire backbone of the aliphatic chain of the 1,6HDT-SAM.^{33,34} Using the estimated heterogeneous

SCHEME 1: Schematic Representation of the Three-Step Electron-Transfer Process Taking Place at the Au-1,6HDT-AuNR Modified Electrodes in an Aqueous Solution Containing 0.1M NaClO₄ and 0.0005 M $[\text{Fe}(\text{CN})_6]^{3-/4-}$

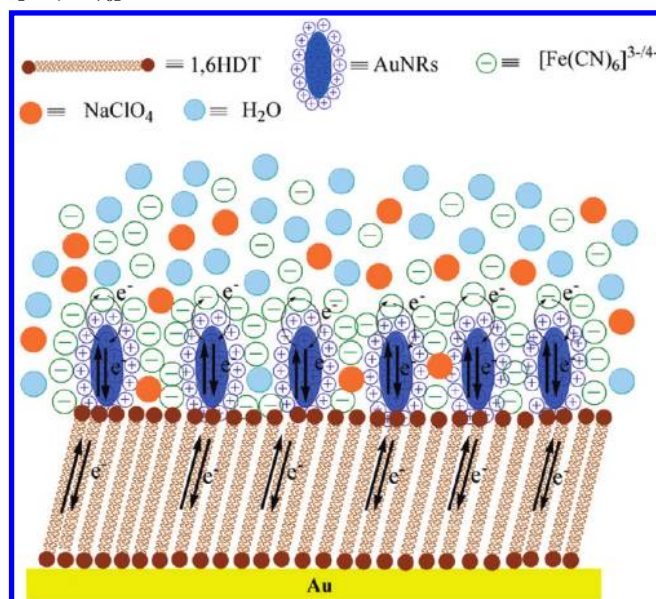


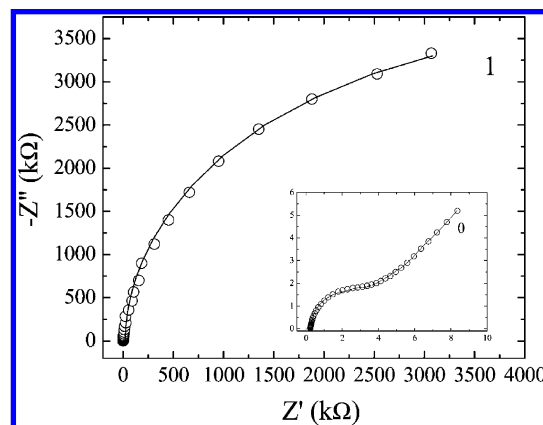
TABLE 2: Heterogeneous Electron-Transfer Rate Constants Calculated for Each Self-Assembled Layer Using the $R_{CT}^{(app)}$ Parameters Obtained from the Fittings of the EIS Spectra and Based on eqs 3–5

n	k_{et} (cm \times s $^{-1}$)	self-assembly time (h)
1	$(0.74 \pm 0.05) \times 10^{-8}$	14
Au NR ₁ terminated bilayer		
2a ₁	$(1.51 \pm 0.02) \times 10^{-5}$	5
2a ₂	$(1.58 \pm 0.03) \times 10^{-5}$	7
2a ₃	$(1.49 \pm 0.02) \times 10^{-5}$	15
2a ₄	$(0.70 \pm 0.04) \times 10^{-5}$	24
Au NR ₂ terminated bilayer		
2b ₁	$(0.72 \pm 0.02) \times 10^{-5}$	5
2b ₂	$(1.00 \pm 0.05) \times 10^{-5}$	15
2b ₃	$(0.44 \pm 0.01) \times 10^{-5}$	24

TABLE 3: Estimated Values of the Tunneling Parameter, β , at Au-1,6HDT-SAM and Au-1,6HDT-AuNR Modified Electrodes As a Function of the Self-Assembly Time of AuNRs

n	β (\AA^{-1})	β_{m} (\AA^{-1})
Au NR ₁ terminated bilayer		
2a ₁	0.7625	0.78 ± 0.08
2a ₂	0.7583	
2a ₃	0.7638	
2a ₄	0.8395	
Au NR ₂ terminated bilayer		
2b ₁	0.8365	0.84 ± 0.10
2b ₂	0.8039	
2b ₃	0.8857	

electron-transfer rate constant, k_{et} , the electron-transfer rate constant at the bare electrode, k_0 , which is 0.031 cm s^{-1} , and the barrier thickness of $(8 \times 1.25 \text{ Å})$, the electron tunneling coefficient for each bilayer as a function of the chemisorption time of the AuNRs was estimated (Table 3). The average values of the tunneling parameter, β , were $0.78 \pm 0.08 \text{ Å}^{-1}$ (AuNR₁) and $0.84 \pm 0.10 \text{ Å}^{-1}$ (AuNR₂) (Table 3). These values suggest also that the process of electron transfer is faster at Au-1,6HDT-AuNR₁ modified electrodes than at the Au-1,6HDT-AuNR₂ modified electrodes. The tunneling distance is constant and the tunneling parameter, β , is independent of the applied potential. As determined from the AFM images, the surface density of 2.33 aspect ratio rods was slightly lower ($1.78 \times 10^9 \text{ AuNR}_1/\text{cm}^2$) than the surface density of 3.16 aspect ratio rods ($2.80 \times 10^9 \text{ AuNR}_2/\text{cm}^2$) on the electrodes, at the optimal time of self-assembly. Despite this slight difference of density, the short rods exhibited a greater improvement in the electrochemistry of $[\text{Fe}(\text{CN})_6]^{3-/4-}$ at the Au-1,6HDT-AuNR modified electrodes (higher increase of peak currents and lower peak separations in the CVs, higher k_{et} values) than the long rods (Figures 5 and 6 and Table 2). Taking into account the fact that the surface densities of the AuNRs were similar, in this situation, the size of the nanorods prevails in the electrochemical process. Moreover, the electron-transfer process is slightly slower at electrodes modified with long rods (Figure 6), but their high density on the substrates assures a very efficient electron-transfer process as compared with the same rods bonded in a side surface topography to the modified substrates (compare curve 2c in Figure 6 of ref 24 with curve 2b₂ in Figure 6 of this paper). This could be due to the fact that, in an end-bonding topography (vertically aligned to the surface), the gold nanorods of both sizes have all their active surface area exposed to the bulk solution. In other words, the charging of the AuNRs by the $[\text{Fe}(\text{CN})_6]^{3-/4-}$ redox probes in solution is possible on both sides

**Figure 7.** Nyquist plots of the bare gold ($n = 0$) and the Au-1,6HDT-SAM ($n = 1$) modified gold electrode in an aqueous 0.1 M NaClO₄ solution containing 0.0005 M $[\text{Fe}(\text{CN})_6]^{3-}$ and 0.0005 M $[\text{Fe}(\text{CN})_6]^{4-}$. The experimental data are represented by circles, and the theoretical curves calculated using the parameter values in Table 4 are represented by solid lines.

of the rods, whereas in a side surface topography, only one side is exposed to the bulk solution. In consequence, each individual AuNR could act as a nanoelectrode. The nanosize of an electrode implies a catalytic effect within the electrochemical process. This feature appears due to the high surface area/volume ratio, specific to nanomaterials.¹¹ As mentioned previously, the density of the rods is highly increased by increasing the solution temperature during their self-assembly process (Figure 1 and Figures S4 and S5 in the Supporting Information). In consequence, the surface of the AuNR-modified electrodes is actually an array of nanoelectrodes. This explains the highly improved electrochemical behavior of the Au-1,6HDT-AuNR modified electrodes toward $[\text{Fe}(\text{CN})_6]^{3-/4-}$ redox probes in solution (Figures 5 and 6).

Electrochemical impedance spectroscopy measurements were performed in order to obtain an additional characterization of Au-1,6HDT-AuNR modified electrodes. The Nyquist plots of the bare gold ($n = 0$), Au-1,6HDT-SAM modified electrode ($n = 1$), Au-1,6HDT-AuNR₁ modified electrode ($n = 2a_{1-4}$), and Au-1,6HDT-AuNR₂ modified electrode ($n = 2b_{1-3}$), respectively, are presented in Figures 7 and 8. The fittings of the EIS spectra were performed using the nonlinear least-squares fit (the Boukamp software), the Randles circuit (for $n = 0$), or the equivalent electrical circuit represented in Figure 9 (for $n = 1, 2a_{1-4}, 2b_{1-3}$). The surface coverage of the 1,6HDT-SAM was 99.93% of the electrode area,²⁴ which implies that the Au electrode surface is covered almost completely with the dithiol molecules.

The impedance responses varied with the chemisorption time and the size of AuNRs. At both types of electrodes, the impedance responses were several orders of magnitude lower in the presence of AuNRs exhibiting semi-infinite planar diffusion at low frequencies (slope unity in the Nyquist plots, Figure 8) as compared with the impedance response recorded at the Au-1,6HDT-SAM modified electrode (Figure 7, $n = 1$). The apparent charge-transfer resistance $R_{CT}^{(app)}$ decreased 3 orders of magnitude upon AuNR self-assembly (Table 4). Comparing the electrochemical behavior of Au-1,6HDT-AuNR modified electrodes, it was observed that the apparent charge-transfer resistance decreased with the size of the nanorods incorporated into the bilayers, the EIS spectra showing smaller semicircles at high and intermediated frequencies at the Au-1,6HDT-AuNR₁ modified electrodes (38.20 nm/16.40 nm rods, Figure 8a) than at the Au-1,6HDT-AuNR₂ modified electrodes (50 nm/15.82

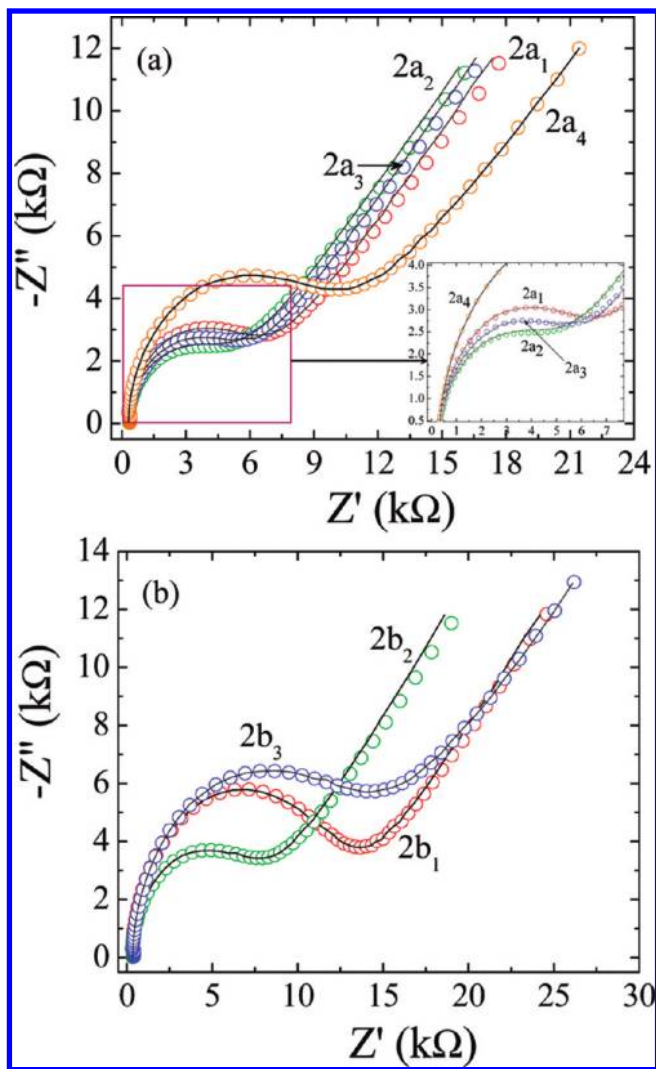


Figure 8. (a) Nyquist plots of Au-1,6HDT-AuNR₁ modified electrodes in an aqueous 0.1 M NaClO₄ solution containing 0.0005 M [Fe(CN)₆]³⁻ and 0.0005 M [Fe(CN)₆]⁴⁻. The chemisorption times of AuNR₁ onto Au-1,6HDT-SAM electrodes were 5 h ($n = 2a_1$, red circles), 7 h ($n = 2a_2$, green circles), 15 h ($n = 2a_3$, blue circles), and 24 h ($n = 2a_4$, orange circles). (b) Nyquist plots of Au-1,6HDT-AuNR₂ modified electrodes in an aqueous 0.1 M NaClO₄ solution containing 0.0005 M [Fe(CN)₆]³⁻ and 0.0005 M [Fe(CN)₆]⁴⁻ for 5 h ($n = 2b_1$, red circles), 15 h ($n = 2b_2$, green circles), and 24 h of chemisorption of AuNR₂ ($n = 2b_3$, blue circles). The theoretical curves, represented by solid lines, have been calculated using the parameter values in Table 4.

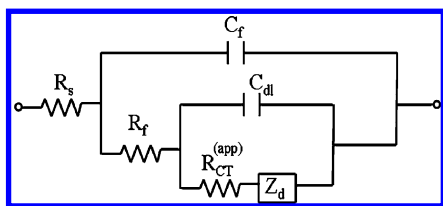


Figure 9. Equivalent electrical circuit used for the fitting of impedance spectra represented in Figures 7 and 8.

nm rods, Figure 8b). The lowest resistance to the charge transfer was estimated for 7 h of chemisorption time of AuNR₁ and for 15 h of chemisorption time of AuNR₂. This is consistent with the cyclic and square wave voltammetry measurements for which the highest increase of peak currents and decrease of peak separation were observed at the same AuNR chemisorption times (Figures 5 and 6, $n = 2a_2$, $2b_2$). This means that, for these times of self-assembly, the surface density of the positively

TABLE 4: Parameter Values Obtained from the Fittings of the Impedance Spectra Represented in Figures 7 and 8 Using the Nonlinear Least-Square Fit^a

n	R_s (kΩ)	C_f (μF)	R_f (kΩ)	C_{dl} (μF)	R_{CT} (kΩ)
0	0.298 (0.32)			0.854 (0.53)	1.595 (0.98)
1	0.295 (0.56)	0.075 (0.51)	3.625 (0.36)	0.142 (0.96)	2.298 (1.05)
Au NR ₁ terminated bilayer					
2a ₁	0.293 (1.09)	0.811 (0.50)	4.917 (1.03)	1.918 (0.76)	1.120 (1.19)
2a ₂	0.300 (1.31)	1.082 (0.68)	3.865 (0.97)	2.983 (0.75)	1.075 (1.05)
2a ₃	0.297 (0.96)	0.992 (0.53)	4.193 (0.41)	1.928 (0.78)	1.135 (1.25)
2a ₄	0.300 (1.05)	1.126 (0.90)	7.283 (0.38)	1.997 (1.62)	2.421 (0.75)
Au NR ₂ terminated bilayer					
2b ₁	0.301 (1.15)	0.397 (0.43)	9.914 (1.75)	1.392 (0.41)	2.345 (0.57)
2b ₂	0.292 (1.32)	0.981 (0.65)	5.652 (1.02)	1.983 (0.96)	1.697 (0.53)
2b ₃	0.305 (1.02)	1.018 (0.70)	8.532 (0.98)	1.657 (1.50)	3.840 (0.84)

^a The percent errors from the fit for each element are given in parentheses.

charged rods, well separated on the substrates, assures a maximum increase of [Fe(CN)₆]^{3-/4-} concentration at the Au-1,6HDT-AuNR/solution interface through electrostatic attraction and an efficient electron transfer across the rods (Scheme 1). Longer chemisorption times induced an increase of the $R_{CT}^{(app)}$ due to the aggregation of the rods within the bilayers (Supporting Information, Figure S4). Despite this aggregation, the bilayers maintained a good electrocatalytic activity toward the [Fe(CN)₆]^{3-/4-} redox probes in solution (Figures 5 and 6, $n = 2a_4$, $2b_3$) as compared to the 1,6HDT monolayer. The capacitance of the films, C_{film} , increased with the chemisorption time of the AuNRs, indicating a continuous increase of electrode areas (Table 4). This is in agreement with the AFM measurements that showed increasing surface coverage with increasing chemisorption times of AuNRs (Figure 1 and Figures S4 and S5 in the Supporting Information). Interestingly, the resistance of the films, R_{film} , which acts as a tunneling resistance for this type of modified electrodes, followed the same trend as the charge-transfer resistance parameter. R_{film} decreased until the optimal time of AuNR self-assembly, proving the presence of an optimal number of electron tunneling channels. This is consistent with the work of Diao et al.,³⁷ for example, who have demonstrated that a higher particle density leads to more tunneling channels, then a smaller apparent tunneling resistance, and more reversible CV behaviors. They have studied the electrochemical properties of 13 nm citrate-stabilized AuNPs immobilized on gold electrodes using 11-amino-1-undecanethiol without reaching AuNP aggregation on the modified electrodes.³⁷ Between 15 and 24 h of self-assembly of the AuNR₁ on the Au-1,6HDT-SAM modified electrodes, R_{film} increased progressively due to the clustering of these rods within the bilayers. The longer rods showed a slower increase of the R_{film} with increasing surface density. This variation of the R_{film} implies that the electrochemical kinetics is controlled not only by a coherent electron tunneling process from the AuNR layers through the 1,6HDT monolayer and toward the underlying Au electrode but also by the density of the AuNRs on the substrates. Additionally, the size of the AuNRs appears to have an influence on these

parameters because a more pronounced increase of $R_{\text{CT}}^{\text{(app)}}$ and R_{film} was observed at the electrodes modified with long rods than at the ones modified with short rods (Table 4). This is consistent with the work of Hu et al., for example, who have studied the size influence of citrate-stabilized AuNPs electrostatically self-assembled on gold electrodes using positively charged myoglobin (Mb).¹⁸ They have found that smaller-sized AuNPs provided more active binding sites for Mb adsorption and demonstrated smaller EIS resistance or better conductivity than that of larger-sized AuNPs.¹⁸ The capacitance of the double layer, C_{dl} , varied as a function of the insulating or conducting properties of each layer self-assembled on Au electrodes. Overall, the electrochemical properties of these bilayers are highly improved as compared with our previous study on the same type of films that were fabricated at a lower solution temperature of the rods (27 °C) and with the addition of 0.2% ethanol.²⁴ Although the size effect of the rods vertically attached to the Au-1,6HDT-SAM electrodes is still present, the highly increased surface density of the 2.33 or 3.16 aspect ratio rods on the electrodes' surface generated quasi-reversible cyclic and square wave voltammograms, with high peak currents and decreased peak separation. For example, the heterogeneous electron-transfer rate constant increased almost 9 times at the Au-1,6HDT-AuNR₁ modified electrode ($k_{\text{et}} = 1.58 \times 10^{-5} \text{ cm} \times \text{s}^{-1}$, Table 2, $n = 2a_2$) as compared with the same type of modified electrode having low surface coverage ($k_{\text{et}} = 0.18 \times 10^{-5} \text{ cm} \times \text{s}^{-1}$, $n = 2a$, ref 24). Moreover, a change of topography from side surface bonding to end surface bonding for the long rods induced a 34 times increase of the heterogeneous electron-transfer rate constant from $k_{\text{et}} = 0.29 \times 10^{-6} \text{ cm} \times \text{s}^{-1}$ ($n = 2c$, ref 24) to $k_{\text{et}} = 1.00 \times 10^{-5} \text{ cm} \times \text{s}^{-1}$ (Table 2, $n = 2b_2$). This increase of the k_{et} demonstrates that the vertical bonding of the AuNRs to the Au-1,6HDT-SAM with a high surface coverage is improving the electrochemical behavior of the modified electrodes. Further research work will be focused on the sensing applications of these films.

4. Conclusions

We have demonstrated that, by increasing the solution temperature of gold nanorods during their self-assembly process to 1,6-hexanedithiol-modified Au electrodes, we can increase the surface density of the rods within the bilayers and change their surface topography. These physical properties of the bilayers had an important influence on the electrocatalytic properties of the resulting Au-1,6HDT-AuNR modified electrodes toward the $[\text{Fe}(\text{CN})_6]^{3-/4-}$ probes in solution. The modified electrodes showed quasi-reversible cyclic and square wave voltammograms with high peak currents and decreased peak separation, indicating a good recovery of the electrochemistry of $[\text{Fe}(\text{CN})_6]^{3-/4-}$ redox probes at the AuNR-modified electrodes. The fastest electron transfer was recorded at the electrodes functionalized with short rods, for a chemisorption time of 7 h, or with long rods, for a chemisorption time of 15 h. The changes in the impedance spectra were associated with the changes in the charge-transfer resistance, film resistance, film capacitance, and electron tunneling across the 1,6HDT monolayer. The charge-transfer resistance decreased with the size of the rods. Within the same bilayer, the charge-transfer resistance increased with the surface density of the rods. The overall decrease of the charge-transfer resistance upon AuNR adsorption to the Au-1,6HDT-SAM electrodes was rationalized in terms of an increase of the concentration of the $[\text{Fe}(\text{CN})_6]^{3-/4-}$ redox probes at the Au-1,6HDT-AuNR/solution interface, charging of the rods, electron transport through the rods, and a coherent

electron tunneling process through the 1,6HDT molecules toward the underlying Au electrode.

Acknowledgment. Financial support from Fundação para a Ciência e a Tecnologia (FCT) of Portugal through the fellowship number SFRH/BPD/39294/2007 is gratefully acknowledged.

Supporting Information Available: UV-vis spectra, TEM images and size distribution histograms of gold nanorods, QCM measurements, AFM images and cyclic voltammograms recorded at the Au-HDT-SAM, Au-HDT-AuNR₁, and Au-HDT-AuNR₂ modified electrodes in an aqueous solution of 0.1 M NaClO₄. This material is available free of charge via the Internet at <http://pubs.acs.org>.

References and Notes

- (1) Murray, R. W. *Chem. Rev.* **2008**, *108*, 2688–2720, and references therein.
- (2) Zabet-Khosousi, A.; Dhirani, A.-A. *Chem. Rev.* **2008**, *108*, 4072–4124, and references therein.
- (3) Talapin, D. V.; Lee, J. S.; Kovalenko, M. V.; Shevchenko, E. V. *Chem. Rev.* **2010**, *110*, 389–458, and references therein.
- (4) Fendler, J. H. *Chem. Mater.* **1996**, *8*, 1616–1624.
- (5) Decher, G. *Science* **1997**, *277*, 1232–1237.
- (6) Ariga, K.; Hill, J. P.; Ji, Q. *Phys. Chem. Chem. Phys.* **2007**, *9*, 2319–2340.
- (7) Bethell, D.; Brust, M.; Schiffrin, D. J.; Kiely, C. J. *Electroanal. Chem.* **1996**, *409*, 137–143.
- (8) Brust, M.; Bethell, D.; Kiely, C. J.; Schiffrin, D. J. *Langmuir* **1998**, *14*, 5425–5429.
- (9) Brust, M.; Schiffrin, D. J.; Bethell, D.; Kiely, C. J. *Adv. Mater.* **1995**, *7*, 795–797.
- (10) Leibowitz, F. L.; Zheng, W.; Maye, M. M.; Zhong, C.-J. *Anal. Chem.* **1999**, *71*, 5076–5083.
- (11) Daniel, M.-C.; Astruc, D. *Chem. Rev.* **2004**, *104*, 293–346.
- (12) Abdelrahman, A. I.; Mohammad, A. M.; Okajima, T.; Ohsaka, T. *J. Phys. Chem. B* **2006**, *110*, 2798–2803.
- (13) Brennan, J. L.; Branham, M. R.; Hicks, J. F.; Osisek, A. J.; Donkers, R. L.; Georganopolou, D. G.; Murray, R. W. *Anal. Chem.* **2004**, *76*, 5611–5619.
- (14) Ranganathan, S.; Guo, R.; Murray, R. W. *Langmuir* **2007**, *23*, 7372–7377.
- (15) Yamamoto, Y.; Yoshi, N.; Shiigi, H.; Nagaoka, T. *Solid State Ionics* **2006**, *177*, 2325–2328.
- (16) Chirea, M.; Morales, V. G.; Manzanaraes, J. A.; Pereira, C. M.; Gulaboski, R.; Silva, F. J. *Phys. Chem. B* **2005**, *109*, 21808–21817.
- (17) Chirea, M.; Pereira, C. M.; Silva, F. J. *Phys. Chem. C* **2007**, *111*, 9255–9266.
- (18) Zhang, H.; Lu, H.; Hu, N. *J. Phys. Chem. B* **2006**, *110*, 2171–2179.
- (19) Ni, W.; Kou, X.; Yang, Z.; Wang, J. *ACS Nano* **2008**, *2*, 677–686.
- (20) Nehl, C.-L.; Liao, H.; Hafner, J. H. *Nano Lett.* **2006**, *6*, 683–688.
- (21) Vial, S.; Pastoriza-Santos, I.; Pérez-Juste, J.; Liz-Marzán, L. M. *Langmuir* **2007**, *23*, 4606–4611.
- (22) Suzuki, T.; Miyata, H.; Noma, T.; Kuroda, K. *J. Phys. Chem. C* **2008**, *112*, 1831–1836.
- (23) Burda, C.; Chen, X.; Narayanan, R.; El-Sayed, M. A. *Chem. Rev.* **2005**, *105*, 1025–1102.
- (24) Chirea, M.; Cruz, A.; Pereira, C. M.; Silva, A. F. J. *Phys. Chem. C* **2009**, *113*, 13077–13087.
- (25) Nikoobakht, B.; El-Sayed, M. A. *Chem. Mater.* **2003**, *15*, 1957–1962.
- (26) Sauerbrey, G. Z. *Phys.* **1959**, *155*, 206–222.
- (27) Lu, M.; Li, X. H.; Yu, B. Z.; Li, H. L. *J. Colloid Interface Sci.* **2002**, *248*, 376–382.
- (28) Nakanishi, T.; Ohtani, B.; Uosaki, K. *J. Phys. Chem. B* **1998**, *102*, 1571–1577.
- (29) Terzi, T.; Zanardi, C.; Zangognini, B.; Pigani, L.; Seeber, R.; Lukkari, J.; Äärälto, T.; Kankare, J. *J. Phys. Chem. C* **2009**, *113*, 4868–4874.
- (30) Jana, N. R.; Gearheart, L.; Murphy, C. J. *Adv. Mater.* **2001**, *13*, 1389–1393.
- (31) Schrader, M. E.; Loeb, G. *Modern Approach to Wettability*; Plenum Press: New York, 1992.
- (32) Wade, L. G., Jr. *Organic Chemistry*, 4th ed.; Prentice Hall: Upper Saddle River, NJ, 1999; pp 1208–1213.
- (33) Gooding, J. J.; Chou, A.; Liu, J. Q.; Losic, D.; Shapter, J. G.; Hibbert, D. B. *Electrochem. Commun.* **2007**, *9*, 1677–1683.
- (34) Diao, P.; Liu, Z. F. *J. Phys. Chem. B* **2005**, *109*, 20906–20913.
- (35) Chidsey, C. E. D. *Science* **1991**, *251*, 919–922.
- (36) Xu, J.; Li, H. L.; Zhang, Y. *J. Phys. Chem.* **1993**, *97*, 11497–11500.
- (37) Diao, P.; Guo, M.; Zhang, Q. *J. Phys. Chem. C* **2008**, *112*, 7036–7046.